Continuously Stirred Decanting Reactor: Operability and Stability Considerations

J. Khinast and D. Luss
Dept. of Chemical Engineering, University of Houston, Houston, TX 77204

M. P. Harold
DuPont Central Research and Development, Wilmington, DE 19880

J. J. Ostermaier and R. McGill
DuPont Nylon, Wilmington, DE 19880

A continuously stirred decanting reactor (CSDR) is a well-mixed vessel fed with two immiscible liquid phases, while its effluent consists of a single phase containing the reaction products. We consider a CSDR in which a desired highly exothermic reaction occurs in one phase, while an undesirable exothermic side reaction occurs in the second extracting phase. The holdup of the two phases in the CSDR is sensitive to its temperature. Thus, the reactor has to be kept in a narrow temperature range to avoid breakthrough, that is, with effluent containing both phases, and to maintain a high selectivity of the desired product. Pilot-plant data for a proprietary selective-oxidation process verified the predictions of the steady-state model.

A high rate of heat generation may lead to various exotic and undesired periodic and aperiodic oscillations, which may shift the reactor out of the region of safe operation and have deleterious impact on the decantation efficiency. In some cases, the oscillations lead to a breakthrough during part of the period. To avoid these oscillatory states, one may have to maintain a sufficiently small difference between the reactor and coolant temperatures. We show how loci of local and global singular points of codimension 1 and 2 can be used to construct maps of parameter regions with qualitatively different steady-state and dynamic bifurcation diagrams. These maps clearly describe the desirable regions of operation and point out all the potential stability and operability issues in other regions.

Introduction

Increasing global competition in the chemical process industry has motivated the development of new and more efficient chemical processes. Multifunctional chemical reactors, combining one or more unit operations with the reaction, offer the potential for simpler chemical processes, higher single-pass yields, and lower energy consumption (Westerterp, 1992). Important commercial chemical processes involve liquid–liquid reactions, such as nitration and/or oxidation of hydrocarbons with nitric acid, sulfonation of hydrocarbons with sulfuric acid, and oxidation of hydrocarbons with hydrogen peroxide (Warwel and Klass, 1994). The presence of two or more liquid phases complicates the design, scale-up, and operation of these reactors. On the other hand, separation schemes may exploit the multiphase feature. For example, one liquid phase may extract a product formed in the other. Extractive reactors may reduce process complexity and size, total investment, and variable costs. Trambouze and coworkers (Trambouze and Piret, 1960; Piret et al., 1960; Trambouze et al., 1961; Trambouze, 1961) developed the theoretical framework for isothermal extractive reactors for both single- and consecutive-reaction systems. They showed that selective extraction may increase the conversion of a reversible reaction or the yield of a desired intermediate. Kollar (1994) described the homogeneously catalyzed oxidation of cyclo-

hexane to adipic acid in the presence of an immiscible acetic acid phase. The high solubility of adipic acid in the polar acetic acid phase enables its extraction before being converted to undesirable byproducts.

Harold et al. (1996) described a novel liquid–liquid extractive reactor, the continuously stirred decanting reactor (CSDR), in which both a single liquid–liquid reaction and extraction/decantation are carried out in a single device. The key characteristic of the reactor is that two liquid phases are fed, but only one is removed. The reaction occurs in the light phase, and the products are soluble only in the heavy phase, which is continuously decanted. This characteristic, combined with the exothermic and activated nature of certain reactions, presents challenging issues concerning reactor operability and stability. Harold et al. (1996) studied the steady-state and dynamic behavior of the particular case of an internally cooled CSDR in which a single exothermic reaction occurred. A unique stable steady state exists in that CSDR, as the heat-generation rate (i.e., product of the feed rate of the light phase times its heat of reaction) is constant.

Here, we extend that analysis of the CSDR to cases in which a consecutive undesirable reaction in the heavy phase may consume the extracted product, and we present a more realistic decantation model. Data from a proprietary selective hydrocarbon oxidation in a pilot-plant decanting reactor are used to verify the validity of the steady-state model. We then describe a systematic method for predicting the dependence of the steady-state and dynamic features on an operating condition and/or design variable. Examples reveal the strong impact of the cooling capacity on the reactor stability and decantation feasibility as well as the existence of complex oscillatory states, which may preclude operation over a wide range of operating conditions for which a desirable steady-state solution exists. Simulations reveal that transitions to chaotic behavior may occur.

A safe, stable, and high-yield operation of the CSDR is feasible only for certain operating conditions. At low temperatures, the high holdup of the lighter phase, which is consumed by the reactions, may lead to phase inversion or even a highly undesired breakthrough of this phase, requiring a reactor shutdown. At high temperatures, the undesired reaction in the extracting phase decreases the selectivity of the desired product, and runaway to even higher temperatures may occur. The instability of the states that satisfy the slope condition may lead to unsafe oscillatory behavior with high-temperature amplitudes. Therefore, it is important to develop a systematic method for mapping the regions with desirable steady-state and dynamic features.

Model Development

We consider a CSDR (Figure 1), fed by two liquid phases. The lighter-phase I feed contains an organic reactant A, an inert component C, and possibly a small amount of oxidant B. The heavier aqueous phase-II feed contains the oxidant B, product E, and possibly small amounts of the desired product D. Reactant A is insoluble in phase II, while reactant B is soluble in both phases. The reaction products D, E, and F are insoluble in the reactive phase and transfer instantaneously upon formation to phase II. The inert C, which may serve as a selectivity-promoting agent, is soluble in both

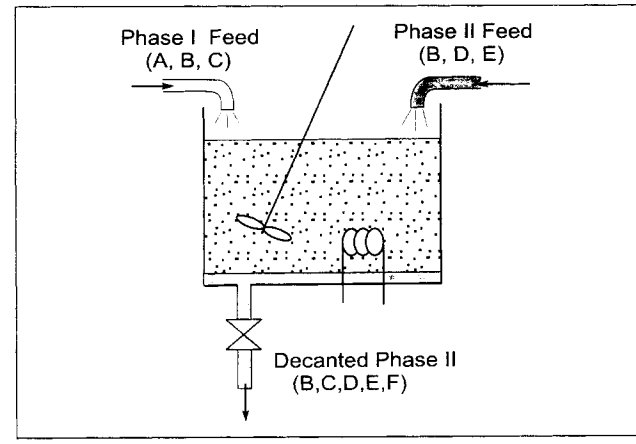

Figure 1. Schematic of a CSDR.

phases. Two exothermic reactions occur in the reactor. In phase I,

$$\nu_{A,1}A + \nu_{B,1}B \rightarrow \nu_{D,1}D + \nu_{E,1}E \tag{1}$$

$$r_1 = k_1(E_1/R)\exp\left\{1 - \frac{E_1}{RT}\right\}c_{A,1}\cdot c_{B,1}, \tag{2}$$

and in phase II

$$\nu_{B,2}B + \nu_{D,2}D \rightarrow \nu_{E,2}E + \nu_{F,2}F \tag{3}$$

$$r_2 = k_2(E_1/R)\exp\left\{\frac{E_2}{E_1}\cdot\left(1 - \frac{E_1}{RT}\right)\right\}\cdot c_{B,\mathrm{II}}\cdot c_{D,\mathrm{II}}. \tag{4}$$

The undesired exothermic reaction between B and the extracted product D in phase II causes a loss of yield. Only phase II is continuously removed from the reactor under normal CSDR operation. A proportional integral (PI) controller adjusts the effluent flow rate to maintain a prescribed liquid holdup in the CSDR. The mathematical model consists of species material balances in phases I and II, an overall energy balance, and an effluent flow-control policy.

The model of phase I consists of species balances for A, B, and C, and a balance on the fractional volume occupied by the three species. The three molar balances in phase I satisfy the equations

$$\frac{d(c_{i,1}V_{\mathrm{I}})}{dt} = \dot{Q}_{\mathrm{I},f}c_{i,\mathrm{I},f} - \dot{Q}_{\mathrm{I,out}}c_{i,1} + \nu_{i,1}\cdot r_1\cdot V_{\mathrm{I}} + \alpha_i k_m a\left(c_{i,\mathrm{II}} - \frac{c_{i,1}}{H_i}\right)(V_{\mathrm{I}} + V_{\mathrm{II}}) \quad i = A,B,C, \tag{5}$$

where $\dot{Q}_{\mathrm{I},f}$ and $\dot{Q}_{\mathrm{I,out}}$ are the volumetric feed and effluent flow rates of phase I, and α_i equals unity for components B and C and zero for A, which is insoluble in phase II.

We assume that the interphase area per unit reactor volume and the holdups of the two phases satisfy the relation

$$a = 4a_0\frac{V_{\mathrm{I}}\cdot V_{\mathrm{II}}}{(V_{\mathrm{I}} + V_{\mathrm{II}})^2}. \tag{6}$$

Under normal CSDR-operation conditions, $\dot{Q}_{\mathrm{I,out}}$ equals zero. Assuming ideal solution behavior, the sum of the fractional volumes occupied by species A, B, and C in phase I satisfy the relation

$$c_{A,\mathrm{I}}\hat{V}_A + c_{B,\mathrm{I}}\hat{V}_B + c_{C,\mathrm{I}}\hat{V}_C = 1. \tag{7}$$

The molar balances of the five species (B, C, D, E, F) in phase II are:

$$\frac{d(c_{B,\mathrm{II}}V_{\mathrm{II}})}{dt} = \dot{Q}_{\mathrm{II},f}c_{B,\mathrm{II},f} - \dot{Q}_{\mathrm{II,out}}c_{B,\mathrm{II}} - k_m a\left(c_{B,\mathrm{II}} - \frac{c_{B,\mathrm{I}}}{H_B}\right)(V_{\mathrm{I}} + V_{\mathrm{II}}) + \nu_{B,2}\cdot r_2 \cdot V_{\mathrm{II}} \tag{8}$$

$$\frac{d(c_{C,\mathrm{II}}V_{\mathrm{II}})}{dt} = \dot{Q}_{\mathrm{II},f}c_{C,\mathrm{II},f} - \dot{Q}_{\mathrm{II,out}}c_{C,\mathrm{II}} - k_m a\left(c_{C,\mathrm{II}} - \frac{c_{C,\mathrm{I}}}{H_C}\right)(V_{\mathrm{I}} + V_{\mathrm{II}}) \tag{9}$$

$$\frac{d(c_{D,\mathrm{II}}V_{\mathrm{II}})}{dt} = \dot{Q}_{\mathrm{II},f}c_{D,\mathrm{II},f} - \dot{Q}_{\mathrm{II,out}}c_{D,\mathrm{II}} + \nu_{D,1}r_1\cdot V_{\mathrm{I}} + \nu_{D,2}r_2 V_{\mathrm{II}} \tag{10}$$

$$\frac{d(c_{E,\mathrm{II}}V_{\mathrm{II}})}{dt} = \dot{Q}_{\mathrm{II},f}c_{E,\mathrm{II},f} - \dot{Q}_{\mathrm{II,out}}c_{E,\mathrm{II}} + \nu_{E,1}r_1\cdot V_{\mathrm{I}} + \nu_{E,2}r_2\cdot V_{\mathrm{II}} \tag{11}$$

$$\frac{d(c_{F,\mathrm{II}}V_{\mathrm{II}})}{dt} = \dot{Q}_{\mathrm{II},f}c_{F,\mathrm{II},f} - \dot{Q}_{\mathrm{II,out}}c_{F,\mathrm{II}} + \nu_{F,2}r_2\cdot V_{\mathrm{II}}. \tag{12}$$

Reaction 1 appears in the balances for species D and E, since they transfer instantaneously to phase II. Finally, the sum of the fractional species volumes is unity:

$$c_{B,\mathrm{II}}\hat{V}_B + c_{C,\mathrm{II}}\hat{V}_C + c_{D,\mathrm{II}}\hat{V}_D + c_{E,\mathrm{II}}\hat{V}_E + c_{F,\mathrm{II}}\hat{V}_F = 1. \tag{13}$$

The corresponding overall energy balance is

$$(V_{\mathrm{I}}(\rho c_p)_{m,\mathrm{I}} + V_{\mathrm{II}}(\rho c_p)_{m,\mathrm{II}})\frac{\partial T}{\partial t} = hA_h(T_c - T) + \left(\dot{Q}_{\mathrm{I},f}(\rho c_p)_{m,\mathrm{I},f} + \dot{Q}_{\mathrm{II},f}(\rho c_p)_{m,\mathrm{II},f}\right)\cdot(T_f - T) + (-\Delta H_1)\cdot r_1\cdot V_{\mathrm{I}} + (-\Delta H_2)\cdot r_2\cdot V_{\mathrm{II}}, \tag{14}$$

where

$$(\rho c_p)_{m,\mathrm{I}} = \sum_{i=A,B,C} c_{p,i}c_{i,\mathrm{I}} \quad \text{and} \quad (\rho c_p)_{m,\mathrm{II}} = \sum_{i=B,C,D,E,F} c_{p,i}c_{i,\mathrm{II}}. \tag{15}$$

The dynamic model of the system describes both the desired normal operation and that which follows a breakthrough, when the reactor operates as a two-phase CSTR. To simplify the analysis, we ignore the possible occurrence of phase inversion before a breakthrough happens. We use a phenomenological expression to account for the composition of the effluent leaving the decanter. If the phase-II reactor holdup exceeds a critical value, $\upsilon_{\mathrm{crit},1}$, the effluent consists only of phase II, that is, CSDR operation is established. If the phase-II holdup fraction is below another critical value, $\upsilon_{\mathrm{crit},2}$, breakthrough occurs and the effluent consists of both phases—a shift to a two-phase CSTR operation with effluent volumetric flow rates proportional to the holdup ratios within the reactor. An empirical smooth function is used to describe this transition from a CSDR to CSTR operation. Specifically,

$$\dot{Q}_{\mathrm{I,out}}/\dot{Q}_{\mathrm{II,out}} = \begin{cases} 0 & \text{for} \quad V_{\mathrm{II}}/(V_{\mathrm{I}}+V_{\mathrm{II}}) > \upsilon_{\mathrm{crit},1} \\ f(x)\cdot V_{\mathrm{I}}/V_{\mathrm{II}} & \text{for} \quad \upsilon_{\mathrm{crit},2} < V_{\mathrm{II}}/(V_{\mathrm{I}}+V_{\mathrm{II}}) < \upsilon_{\mathrm{crit},1}, \\ V_{\mathrm{I}}/V_{\mathrm{II}} & \text{for} \quad \upsilon_{\mathrm{crit},2} > V_{\mathrm{II}}/(V_{\mathrm{I}}+V_{\mathrm{II}}) \end{cases} \tag{16}$$

where

$$f = 2x^3 - 3x^2 + 1, \quad x = \frac{V_{\mathrm{II}}/(V_{\mathrm{I}}+V_{\mathrm{II}}) - \upsilon_{\mathrm{crit},2}}{\upsilon_{\mathrm{crit},2} - \upsilon_{\mathrm{crit},1}} \tag{17}$$

A PI-controller attempts to maintain a set total liquid volume in the reactor by adjusting the effluent flow rate so that

$$\dot{Q}_{\mathrm{I,out}} + \dot{Q}_{\mathrm{II,out}} = k_v(V_{\mathrm{I}} + V_{\mathrm{II}}) + k_{\mathrm{int}}\int_0^t [V_{\mathrm{I}}(t') + V_{\mathrm{II}}(t') - V_S]\,dt'. \tag{18}$$

The 13 model equations (5, 7–14, 16, 18) describe 13 variables—five in phase I ($c_{A,\mathrm{I}}$, $c_{B,\mathrm{I}}$ $c_{C,\mathrm{I}}$, V_{I}, $\dot{Q}_{\mathrm{I,out}}$), seven in phase II ($c_{B,\mathrm{II}}$, $c_{C,\mathrm{II}}$, $c_{D,\mathrm{II}}$, $c_{E,\mathrm{II}}$, $c_{F,\mathrm{II}}$, V_{II}, $\dot{Q}_{\mathrm{II,out}}$), and the temperature T. Introducing the dimensionless variables

$$u_{A,\mathrm{I}} = \frac{c_{A,\mathrm{I}}}{c_{A,\mathrm{I},f}}; \quad u_{B,\mathrm{I}} = \frac{c_{B,\mathrm{I}}}{H_B\cdot c_{B,\mathrm{II},f}}; \quad u_{C,\mathrm{I}} = \frac{c_{C,\mathrm{I}}}{c_{C,\mathrm{I},f}};$$

$$u_{B,\mathrm{II}} = \frac{c_{B,\mathrm{II}}}{c_{B,\mathrm{II},f}}; \quad u_{C,\mathrm{II}} = \frac{c_{C,\mathrm{II}}}{c_{C,\mathrm{I},f}/H_C}$$

$$u_{D,\mathrm{II}} = \frac{c_{D,\mathrm{II}}}{c_{B,\mathrm{II},f}}; \quad u_{E,\mathrm{II}} = \frac{c_{E,\mathrm{II}}}{c_{E,\mathrm{II},f}}; \quad u_{F,\mathrm{II}} = \frac{c_{F,\mathrm{II}}}{c_{B,\mathrm{II},f}};$$

$$q_{\mathrm{I}} = \frac{\dot{Q}_{\mathrm{I,out}}}{\dot{Q}_{\mathrm{I},f}}; \quad q_{\mathrm{II}} = \frac{\dot{Q}_{\mathrm{II,out}}}{\dot{Q}_{\mathrm{II},f}}$$

$$\Omega_{\mathrm{I}} = \frac{V_{\mathrm{I}}}{V_t}; \quad \Omega_{\mathrm{II}} = \frac{V_{\mathrm{II}}}{V_t}; \quad \omega = \frac{\dot{Q}_{\mathrm{I},f,R}t}{V_t}; \quad \Theta = \frac{TR}{E_1} \tag{19}$$

and the dimensionless groups

$$Da_1(\tau_R) = k_1(E_1/R)H_B c_{B,\mathrm{II},f}\tau_R;$$

$$Da_2(\tau_R) = k_2(E_1/R)c_{B,\mathrm{II},f}\tau_R; \qquad \tau_R = \frac{V_t}{\dot{Q}_{\mathrm{I},f,R}};$$

$$\frac{\tau}{\tau_R} = \frac{\dot{Q}_{\mathrm{I},f,R}}{\dot{Q}_{\mathrm{I},f}}; \qquad Da_i(\tau) = Da_{i,R}\cdot\frac{\tau}{\tau_R}; \qquad \beta_1 = \frac{-\Delta H_1 R}{c_{pA}E_1};$$

$$\beta_2 = \frac{-\Delta H_2 R}{c_{pA}E_1}; \ \sigma = \frac{E_2}{E_1} \tag{20}$$

$$P_1 = \frac{\dot{Q}_{\mathrm{II},f,R}}{\dot{Q}_{\mathrm{I},f,R}}; \qquad P_{2,R} = k_m\cdot a\cdot\tau_R; \qquad P_{3,R} = \frac{k_v}{P_1}\cdot\tau_R;$$

$$P_3(\tau) = P_{3,R}\cdot\frac{\tau}{\tau_R}; \qquad P_{4,R} = \frac{k_{\mathrm{int}}}{P_1}\cdot\tau_R^2; \qquad P_4(\tau) = P_{4,R}\cdot\left(\frac{\tau}{\tau_R}\right)^2;$$

$$\Delta_R = \frac{hA_h}{\dot{Q}_{\mathrm{I},f,R}(\rho c_p)_{m,\mathrm{I},f} + \dot{Q}_{\mathrm{II},f,R}(\rho c_p)_{m,\mathrm{II},f}}; \quad \Delta = \Delta_R\frac{\tau}{\tau_R}$$

the model equations are transformed to the dimensionless equations reported in the Appendix. In Eq. 20, τ_R is a reference residence time and Δ_R is a reference cooling capacity.

Our model accounts for all the different types of the steady-state solutions, including those obtained following a breakthrough; that is, when CSDR operation is no more feasible and the reactor becomes a two-phase CSTR. In contrast, the model by Harold et al. (1996) did not account for states attained after a breakthrough occurred. Thus, our model may predict a larger number of steady-state solutions.

Experimental Validation of the Steady-State Model

The validity of the steady-state model predictions was tested by data from a decanting reactor used to evaluate the feasibility of a novel proprietary two-liquid, phase-oxidation process. The two reactions described by Eqs. 1 and 3 occur in the system, where A denotes a hydrocarbon, B a liquid-phase oxidant, C a selectivity modifier that remains unconverted (inert), D a desired oxygenate, E water, and F an undesired byproduct. A is nearly insoluble in the aqueous phase; B is soluble in both the hydrocarbon and aqueous phase. The desired product D is soluble in the aqueous phase and nearly insoluble in the organic phase, and the undesired byproduct F is insoluble in the organic phase. Thus, the first reaction occurs in the organic phase, while the second reaction occurs in the aqueous phase. Both reactions have high heats of reaction and activation energies. Laboratory experiments showed that

$$E/R = T_R = 15{,}000\ \mathrm{K}; \qquad (-\Delta H)\cdot R/(c_{p,HC}\cdot E) = 0.5 \tag{21}$$

for the organic-phase reaction. The corresponding Damköhler numbers defined as the reactor volume divided by the product of the organic phase volumetric feed rate, and the characteristic reaction time at the reaction temperature (about 110°C), were of order unity. The heat of reaction and activation energy of the byproduct reaction were even higher than those of the desired reaction. The reactor is highly sensitive to the temperature and had to be kept below a critical temperature to avoid runaway and boiling.

The nearly immiscible phase distribution and rapid phase-separation features were exploited successfully in a pilot CSDR. Over a narrow temperature range, this CSDR had steady states with complete conversion of the hydrocarbon and a high selectivity of the desired oxygenate, which was continuously recovered in the effluent aqueous stream. Under these conditions, the CSDR may be treated as though only the desired reaction (Eq. 1) occurs. In this case, the composition of the effluent is independent of the reactor temperature. If, in addition, the solubility of B and the inert C are independent of the temperature, or if the experiments are conducted over a narrow temperature range in which the solubilities are essentially constant, then the concentration of all the species in the organic phase are independent of the CSDR temperature. Since in the CSDR the consumption rate of the organic reactant is equal only to its feed rate, the following relation (Harold et al., 1996) must hold:

$$V_{\mathrm{org}} \propto \exp[E/(RT)]. \tag{22}$$

The validity of this model prediction was tested by measuring the dependence of the organic phase (in wt. %) in the pilot CSDR as a function of the temperature. This holdup decreased monotonically from about 45 wt. % at 93°C to 15 wt. % at 105°C. CSDR operation could not be maintained below 90°C because phase inversion occurred, leading to organic-phase appearance in the effluent.

Figure 2 shows that the experimental data fit the Arrhenius temperature dependence predicted by Eq. 22 rather well, with an activation energy of 134,000 kJ/kmol. Independent laboratory kinetic measurements showed that the activation energy of this reaction was in this range. This close agree-

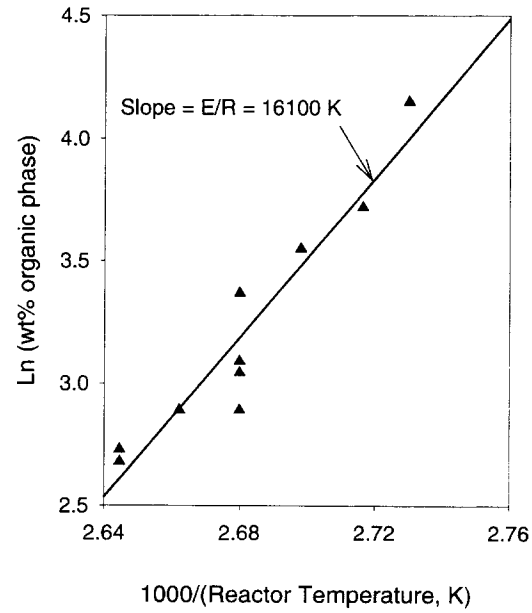

Figure 2. Arrhenius temperature-dependence of wt. % holdup of the organic phase as a function of the reciprocal of the pilot-plant reactor temperature.

The slope corresponds to an activation energy of 134,000 kJ/kmol.

ment supports the validity of the steady-state model-holdup predictions for the single-reaction case. The data point out a rather sensitive dependence of the holdup on the operating temperature. It should be noted that Eq. 22 is only valid in the temperature range in which the desired reaction is the dominant one. Outside that range, undesired reactions in both the aqueous and organic phases will invalidate it.

Methods of Predicting the Model Features

The mathematical model of the CSDR may be written as a set of nonlinear ordinary differential equations, of the form

$$C(u, p, \lambda)\cdot\frac{du}{dt} - f(u, p, \lambda) = 0$$
$$u(t=0) = u_0 \tag{23}$$

where C is a capacitance matrix, f a vector of nonlinear functions, and λ a *distinguished* or *bifurcation parameter*. We briefly review the various loci, which separate parameter regions having qualitatively different steady-state and/or dynamic features. The definitions and methods of calculating these singularities are described in the Appendix.

A *bifurcation diagram* describes the dependence of a state variable upon a continuous change in a bifurcation variable, λ. Two bifurcation diagrams are *qualitatively similar* when the number, order, and orientation of the solutions u change in an identical way upon a continuous change in the bifurcation variable. In general, the number of steady-state solutions changes by two at a *limit point*. A similar change may occur at a breakthrough point, which may be considered as a *generalized limit point*. A dynamic bifurcation analysis determines the parameters at which the dynamic features of the system change. A steady state becomes unstable, and periodic solutions appear at a *Hopf bifurcation*. At that point, a conjugate pair of eigenvalues μ of the linearized system crosses the imaginary axis.

Singular points are defined to be of codimension n, if n parameters including the bifurcation variable have to be varied in order to obtain all the possible qualitatively different features (unfolding) next to the singular point. For example, limit points and Hopf points are codimension 1 singular points; hysteresis, isola, and degenerate Hopf loci are of codimension 2. Bifurcation diagrams obtained by unfolding of all the codimension-2 varieties considered in this article are shown in Figure 3. Typically, two limit points coalesce upon crossing the *hysteresis variety* (HV), while an isolated branch of solutions appears (or disappears) upon crossing the isola variety (I). Crossing of either the hysteresis or the isola variety typically changes by two the number of limit points of the bifurcation diagram. Crossing a double-limit variety (DL) typically changes the relative positions of two limit points in the bifurcation diagram.

In the analysis of the CSDR, one needs to also account for the *boundary limit* variety (BL), defined by Balakotaiah and Luss (1984), where a limit point occurs at the boundary of the bifurcation parameter. Here, we define a BL variety as the points at which a limit point and breakthrough occur simultaneously, that is, a limit point exists on the boundary of feasible operation. The breakthrough locus separates two models with different physical behavior (normal operation, breakthrough). The low-temperature boundary of multiple solutions is the point at which a breakthrough and a limit point coalesce. The qualitative features of a bifurcation diagram at such a point are similar to those at a hysteresis variety. An *infinite limit* point (IL) is the set of parameters at which a limit point exists as $\lambda \to \infty$.

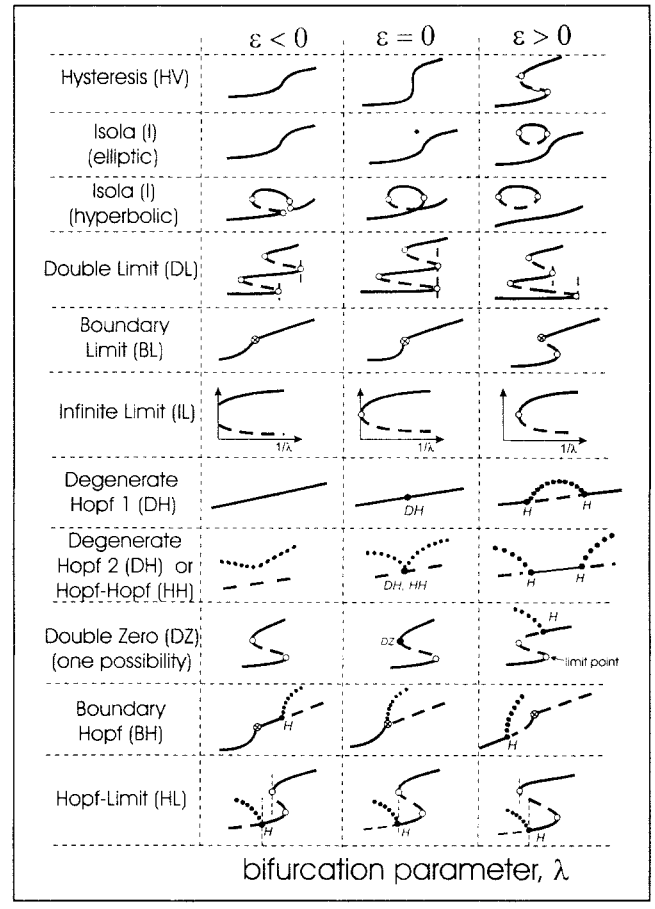

Figure 3. Universal unfolding of the steady-state and dynamic bifurcations of codimension-2 singularities.

H = Hopf point; ⊗ = breakthrough; —— = stable steady state; – – – = unstable steady state; · · · = oscillatory state.

In addition to the steady-state singular points of codimension 2, dynamic singularities of codimension 2 exist. Two Hopf points coalesce at a *degenerate Hopf* point (DH). The bifurcation diagrams obtained by perturbing one parameter of a degenerate Hopf point contain either two Hopf points or none (Figure 3). At a *Hopf – Hopf mode-interaction* point (HH), two distinct conjugate pairs of eigenvalues transversely intersect the imaginary axis (see Figure 3). A Hopf and a limit point coalesce at a *double-zero* point (DZ) (Figure 3), that is, a pair of purely complex conjugate eigenvalues vanishes as they coalesce with the zero eigenvalue of a limit point. At a *boundary-Hopf* locus (BH), a Hopf locus coalesces with the feasible operation boundary (breakthrough).

The qualitative steady-state and dynamic features of a bifurcation diagram may change by crossing either a local or a global bifurcation point. These global bifurcations lead to qualitative changes in the global dynamic features of the

CSDR. For example, a global bifurcation occurs at a *Hopf-limit* point (HL), where a limit point and a Hopf point exist on different solution branches for the same set of parameters. A typical situation is depicted in Figure 3.

We briefly mention the numerical techniques used in this work. The branches of steady-state solutions and the various singular points were computed with respect to a parameter by an arc-length continuation scheme (Keller, 1977). We constructed maps of parameter regions with qualitatively different steady-state and dynamic features by continuing the loci of the singular codimension-2 points with respect to an additional parameter, p_2, in $\boldsymbol{p}$. Lower-order singularities provided an initial guess for higher-order ones. All nonlinear equations were solved by a Newton method. The continuation of the periodic branches of solutions with respect to a parameter was accomplished by transforming the initial-value problem, Eq. 23, into a boundary-value problem, with the period being an additional variable and adding an anchor equation (Kubicek and Marek, 1983).

Impact of Cooling on the CSDR Dynamics

We present some examples to illustrate a CSDR used to carry out the two consecutive reactions described by Eqs. 1 and 3. Loci of various singular points are used to map desirable regions of operation. Numerical simulations lead to insight into the nature of the various possible oscillatory states and the transition to chaotic behavior. Simulations of pilot-plant experiments, some of which were described before, motivated the parameter choice. The values of the parameters used in the simulations are given in Table 1. The critical holdup below which breakthrough occurs was assigned a value of 0.05. This value depends on the liquid-liquid dispersion and the decanter design. We had to change the values of some kinetic parameters due to proprietary considerations. Note that our model does not account for boiling and thus in invalid for very high temperatures, which need to be avoided anyway due to safety considerations.

We first consider a case in which the Damköhler numbers for the two reactions at $T = E_1/R$ are $Da_1(\tau_R) = 10^{11}$ and

Table 1. Parameter Values Used in the Simulation

Parameter	Value	Parameter	Value
$Da_1(\tau_R)$	10^{11}	$Da_2(\tau_R)$	2.5×10^{13}
β_1	0.5	β_2	1.0
P_1	10	$P_{2,R}$	10^4
$P_{3,R}$	1.11	$P_{4,R}$	1.0
T_r	10,000 [K]	σ	1.5
$\nu_{A,1}$; $\nu_{B,2}$; $\nu_{D,2}$	-1	$\nu_{D,1}$; $\nu_{E,2}$; $\nu_{F,2}$	$+1$
$\nu_{B,1}$	-2	$\nu_{E,1}$	$+2$
$c_{A,I,f}/c_{B,II,f}$	1.6	$c_{B,I,f}/c_{B,II,f}$	10^{-5}
$c_{C,I,f}/c_{B,II,f}$	0.4	$c_{C,II,f}/c_{B,II,f}$	0.4×10^{-5}
$c_{D,II,f}/c_{B,II,f}$	10^{-5}	$c_{E,II,f}/c_{B,II,f}$	7.14
$c_{A,I,f}/c_{E,I,f}$	4.0	$c_{C,II,f}/c_{C,I,f}$	10^{-5}
$c_{A,I,f}/c_{E,II,f}$	0.224	$c_{F,I,f}/c_{B,II,f}$	0.0
$c_{A,I,f}\cdot\hat{V}_A$	0.8	c_{pB}/c_{pA}; c_{pC}/c_{pA}; c_{pF}/c_{pA}	1.0
c_{pD}/c_{pA}; c_{pE}/c_{pA}	1.0	Ω_s	0.95
H_B	0.2	H_C	5.0
$\hat{V}_C/\hat{V}_B$	1.67	$\hat{V}_D/\hat{V}_B$	1.2
$\hat{V}_E/\hat{V}_B$	0.33	$\hat{V}_B/\hat{V}_A$	0.6
$\hat{V}_C/\hat{V}_A$	1.0	$\hat{V}_F/\hat{V}_B$	1.2
$\upsilon_{crit,1}$	0.05	$\upsilon_{crit,2}$	0.04

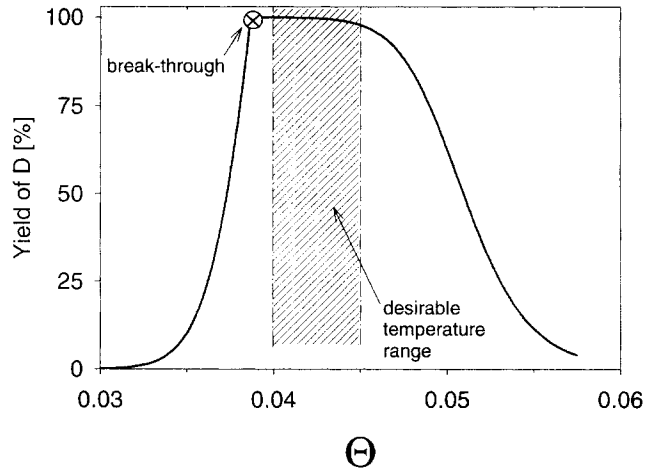

Figure 4. Dependence of the steady-state yield of product D on the reactor temperature, Θ for $\tau = \tau_R$.

It is desirable to operate within the dashed temperature range.

$Da_2(\tau_R) = 2.5\times10^{13}$, and the effective cooling capacity $\Delta = \Delta_R$. Figure 4 describes the steady-state yield of the desired product as a function of the steady-state temperature of the CSDR. It suggests that, in order to maintain a high D yield ($> 98\%$), the CSDR dimensionless temperature should be in the range of $0.04 < \Theta < 0.045$. The lower bound prevents a drift to a breakthrough (extinguished reaction) and the upper one avoids states for which the rate of the undesired second reaction is appreciable. Additionally, high temperatures could lead to runaway due to the initiation of undesired reactions and boiling.

Figure 5 describes the loci of codimension-1 singularities, that is, the limit point, Hopf, and breakthrough loci in the

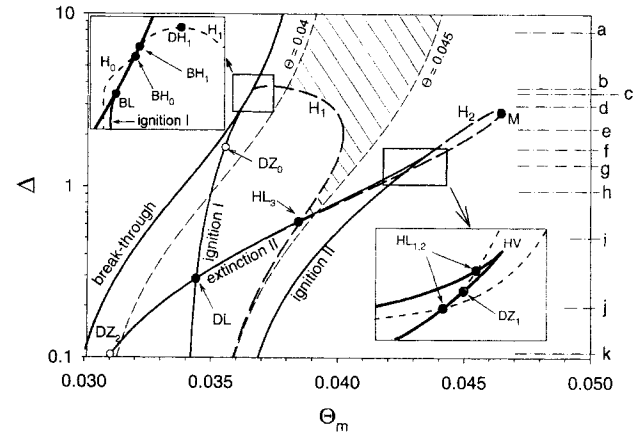

Figure 5. Loci of singular points of codimension 1 (limit, Hopf) and breakthrough points in the Δ vs. Θ_m plane for $\tau = \tau_R$.

H = Hopf; HV = hysteresis, DZ = double-zero; DL = double limit; HL = Hopf-limit; BH = boundary Hopf; BL = boundary limit, DH = degenerate Hopf. The two isotherms bound regions with high yield ($> 98\%$). Unique stable steady states exist in the dashed area. Parameters are specified in Table 1.

plane of the dimensionless cooling capacity Δ vs. the weighted feed and coolant average temperature Θ_m, defined as

$$\Theta_m = \frac{\Theta_f + \Delta \cdot \Theta_c}{1 + \Delta}. \tag{24}$$

When the feed and coolant temperatures are equal, that is, when $\Theta_c = \Theta_f$, then Θ_m is independent of Δ. In all our simulations, we assume that $\Theta_m = \Theta_c = \Theta_f$.

Species A is completely consumed under normal operation of the CSDR, as no breakthrough occurs. Thus, for a given flow rate and feed composition, breakthrough always occurs at the same dimensionless temperature ($\Theta = 0.03867$), as long as the rate of the second reaction is negligible and the reactor temperature changes linearly with the coolant and feed temperature (Harold et al., 1996). Once the rate of the second reaction becomes significant, Θ and Θ_m are not linearly related.

The CSDR has at most five steady-state solutions for the parameters and operating conditions that correspond to Figure 5. Thus, any bifurcation diagram has at most four limit points (ignition I, ignition II, extinction II, and a breakthrough point, which may be considered as a generalized limit point). The projections of the ignition-I and extinction-II limit points intersect and form a DL point. The ignition-I and the breakthrough loci intersect tangentially, forming a BL point, whereas the ignition-II and extinction-II loci form a cusp at the hysteresis locus (HV). Multiple solutions for some Θ_m exist when the cooling capacity Δ is chosen below the BL point, $\Delta = 2.66$.

Three Hopf loci (denoted as H_0, H_1, and H_2) exist in this example. The H_0 locus emanates from the double-zero point DZ_0 and ends at the boundary-Hopf point BH_0. It is very close to the breakthrough and ignition-I loci. Thus, it is not visible in the main part of the figure. The H_1 locus emanates from BH_1, which lies very close to BH_0 (see insert), and the H_2 locus emanates from the double-zero point DZ_1 (see insert) and ends at the double-zero point DZ_2. The projections of the H_1 and H_2 loci intersect the ignition and extinction loci, generating three Hopf-limit points (HL_1, HL_2, and HL_3). Oscillatory states exist for some feed temperatures when the dimensionless cooling capacity is lower than $\Delta = 3.83$ (point DH_1 in Figure 5). Similarly, no oscillatory states exist for inlet temperatures exceeding $\Theta_m = 0.0465$ (point M in Figure 5). However, for such high temperatures, essentially all the feed is converted to the undesired product F.

The loci of $\Theta = 0.04$ and 0.045 in Figure 5 bound operating conditions for which a desirable steady-state solution exists. However, many of these desirable steady states are unstable. A unique, stable stationary state with a yield of at least 98% of the desired product exists within the dashed area in Figures 5, bounded between the H_1, the extinction-II loci and the two limiting-temperature loci. Clearly, increasing the cooling capacity increases the range of Θ_m for which a CSDR has a unique, stable steady state.

Inspection of Figure 5 shows that 11 qualitatively different bifurcation diagrams of Θ vs. Θ_m may be attained for different cooling capacities. The value of Δ corresponding to each case is marked on Figure 5, and the different diagrams are shown in Figure 6. In case a, which corresponds to a relatively high cooling capacity, a unique stable state (solid line)

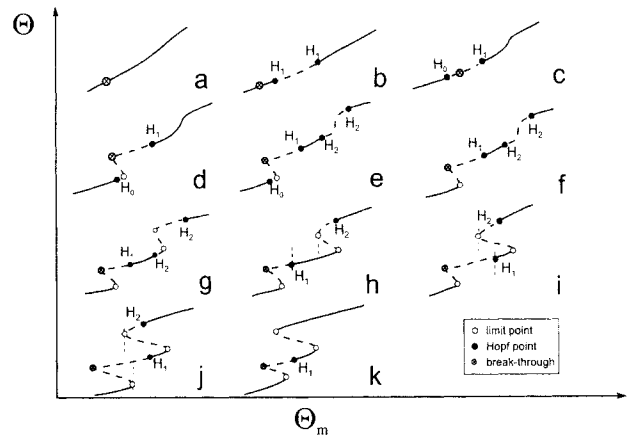

Figure 6. Eleven bifurcation diagrams of Θ vs. Θ_m corresponding to different Δ values, as denoted on the ordinate in Figure 5.

exists for all inlet temperatures, and it is possible to obtain safe operation and a high yield by a proper choice of the feed and cooling temperatures. Some of these states are destabilized (broken line) and become oscillatory for a certain range of feed temperatures (cases (b) and (c)). Oscillations occur only between the two supercritical Hopf points. Further reduction of Δ leads to three types of bifurcation diagrams (cases (d), (e), and (f)) with a 1-3-1 multiplicity. The multiplicity region consists of an undesired low-temperature stable breakthrough branch, an unstable state, and an undesired oscillatory state. Further reduction in the cooling capacity generates bifurcation diagrams with 1-3-1-3-1 multiplicity (cases (g)–(i)), meaning that multiplicity exists in two separate θ_m regions. When the cooling capacity is smaller than that of the HL_3 locus, no unique, stable steady state exists within the desired temperature range. Thus, stable unique states with a high yield of the desired product ($\Theta < 0.045$) exist for cases (g) and (h) for some Θ_m, but not for case (i). For even lower cooling capacities, the two multiplicity regions overlap, giving 1-3-5-3-1 bifurcation diagrams. There are two such types of diagrams (cases (j) and (k)); in each instance, no unique and stable state with a high yield of the product exists. Since the H_1 locus is very close to the $\Theta = 0.045$ isotherm, small perturbations may lead to runaway. Consequently, a desirable state may be obtained in regions (a) to (h) for certain inlet temperatures but not in regions (i) to (k). The boundary between these two cases is the Hopf-limit point HL_3.

The operation of the CSDR should avoid transient temperature excursions due to safety considerations and the deleterious impact on the efficiency of the decanter. In all numerical examples, we found that the Hopf bifurcations were supercritical in the neighborhood of the operational region. Thus, the transition from stationary to oscillatory behavior is determined by the bifurcations described earlier. When the Hopf bifurcations are subcritical, one needs to consider additional bifurcation sets in order to predict regions of safe operation.

An important design decision is the selection of proper cooling capacity and feed and coolant temperature. Figure 7 indicates that for the high cooling capacity of $\Delta = 5$, the high-yield state is stable and unique. Under these conditions,

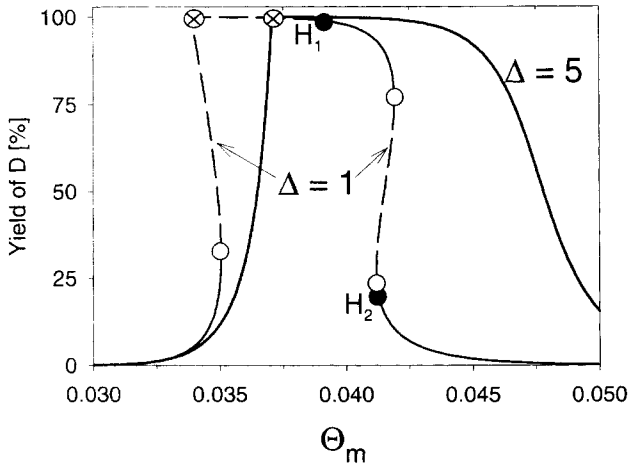

Figure 7. Bifurcation diagrams of the yield of *D* vs. inlet temperature Θ_m for two cooling capacities Δ, denoted as (a) and (h) in Figure 5.

the bifurcation diagram of Θ vs. Θ_m is of the form of Figure 6a. When Δ is reduced to 1, most high-yield states become oscillatory, and the bifurcation diagram takes the form of Figure 6h. A stable steady state needs to satisfy the slope condition—the change in the rate of the heat-removal with temperature must exceed that of the rate of heat generation by the reaction. Figures 5–7 point out that dynamic considerations (the need to avoid oscillatory states) may necessitate much higher cooling capacity than that needed to satisfy the slope condition. Thus, the map of the desired and stable region of operation in Figure 5 is essential for rational design and control of the CSDR.

The nature of the oscillatory states strongly depends on the cooling capacity and the feed and coolant temperatures. Figure 8 is a numerically computed bifurcation diagram that describes the maximal and minimal temperature of the oscillatory states as well as the steady-state behavior as a function of the feed temperature. The branching of the oscillatory states is supercritical. The deviation of the maximal temperature from that of the unstable steady state significantly exceeds that of the minimal temperature (which is close to the coolant temperature) from the unstable state.

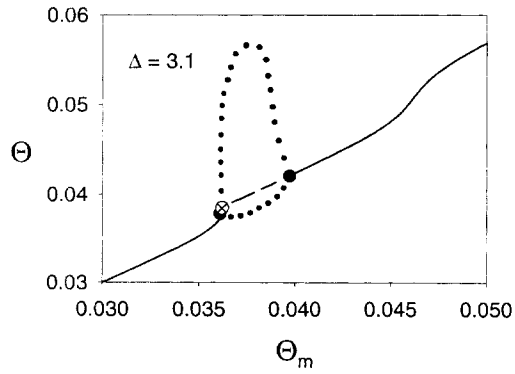

Figure 8. Bifurcation diagram of Θ vs. Θ_m for $\Delta = 3.1$ ((c) in Figure 6).

Dots represent the maximal amplitudes of the stable oscillatory states.

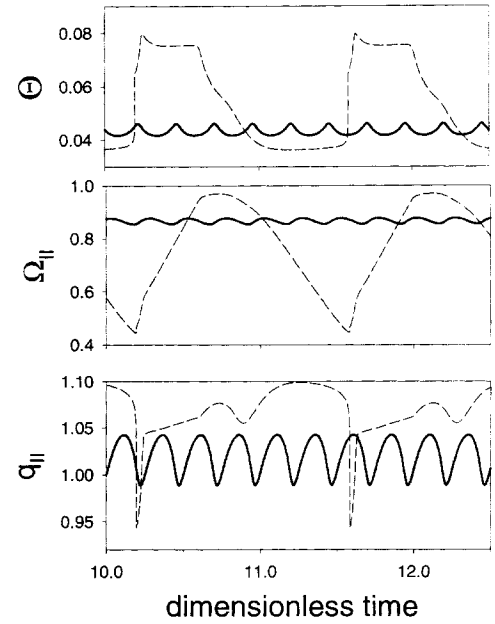

Figure 9. Oscillations of Θ, holdup (Ω_{II}), and effluent flow rate (q_{II}) of the aqueous phase in a CSDR for two parameter sets.

Dashed lines are for $\Delta = 0.4$, $\Theta_m = 0.0357$; solid lines for $\Delta = 2$, $\Theta_m = 0.04$.

Figure 9 shows two typical oscillatory time series of Θ, the dimensionless volume (Ω_{II}), and flow rate (q_{II}) of phase II for two different cases. The solid line in Figure 9 corresponds to a case with a relatively high cooling capacity ($\Delta = 2$) and feed and coolant temperatures of 0.04. The corresponding bifurcation diagram is of type (e) in Figure 6. These oscillations are rather regular and smooth, with a relatively small amplitude. The oscillatory state described by the dashed line in Figure 9 occurs at a lower cooling capacity of $\Delta = 0.4$ and $\Theta_m = 0.0357$. The oscillations are of period 2, and their amplitudes are much higher than those in the first case. Periodic states are usually avoided due to safety concerns and their impact on the decanter. The large-amplitude oscillations may also have a negative impact on the yield of the desired product. For example, the time-average yield of *D* in the first case exceeds 95%, as the oscillation has a small amplitude in the range between $\Theta = 0.04$ and $\Theta = 0.046$. However, in the second case, the high-amplitude oscillations reduce the time-average yield to approximately 20%.

The simulations indicate that in a certain narrow region of operation (Figure 5, to the right of the line BH_0–BL–DZ_0–DL), rather harmful, complex oscillations around a unique unstable steady state can lead to a breakthrough during part of the period. A typical case is shown in Figure 10. Normal CSDR operation ($q_I = 0$) occurs only during a small fraction of the oscillation period, and, most of the time, breakthrough occurs. This may be rather surprising at first, as no steady state with breakthrough exists for this set of operating conditions.

The oscillatory states are usually of period 1 or period 2. In some parameter regions, more intricate oscillations may occur. Since the nonstationary operation of the CSDR is avoided in practice, we mention only briefly some of the complex os-

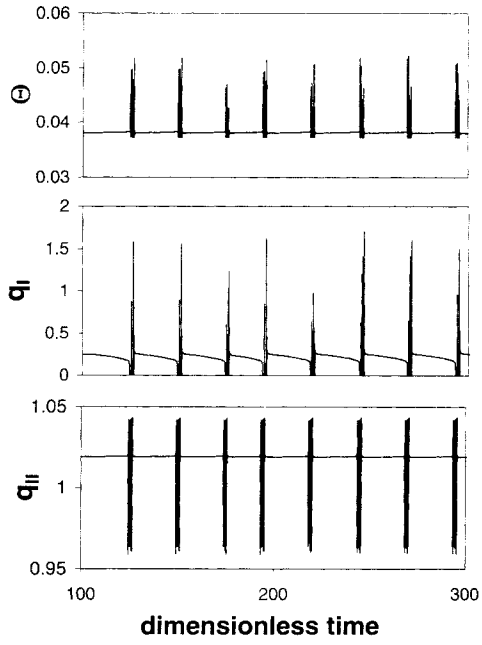

Figure 10. Complex oscillations of Θ and the effluent flow rates of the light (q_I) and heavy phase (q_{II}) around an unstable, unique steady state of the CSDR.

In this case, $\Delta = 0.5$, $\Theta_m = 0.03481$, and $\tau = \tau_R$. The corresponding bifurcation diagram is of type (i) in Figure 6.

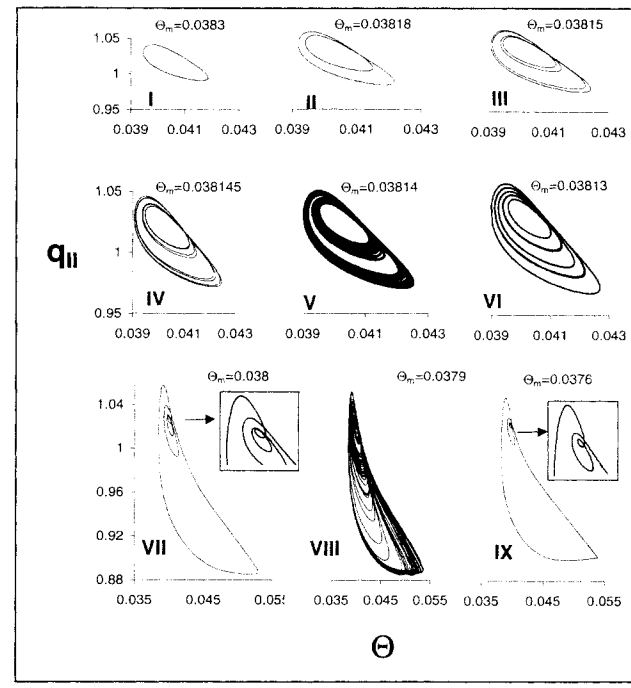

Figure 11. Nine different phase-plane diagrams of the effluent flow rate of phase II (q_{II}) vs. Θ for $\Delta = 3.5$, $\tau = \tau_R$, and different Θ_m values.

cillatory dynamic features that may be encountered when either the cooling capacity and inlet temperature are changed, such as period-doubling cascades, quasi-periodic behavior, and chaotic states. Figure 11 describes nine different phase-plane behaviors observed upon small variations in Θ_m for a constant cooling capacity ($\Delta = 3.5$) and $\tau/\tau_R = 1$. Cases I to IV describe a period-doubling scenario. The oscillations shift from a period-1 limit cycle at $\Theta_m = 0.0383$, to period-2 at $\Theta_m = 0.03818$, to period-4 at $\Theta_m = 0.03815$, and period-8 at $\Theta_m = 0.038145$. In agreement with theoretical predictions (Feigenbaum, 1983), the interval of Θ_m for which a $2n$ period exists decreases as n increases. Further reduction of Θ_m leads to period 16, period 32, and eventually to a quasi-periodic or chaotic behavior. The simulations reveal that several strange attractors exist for various windows of Θ_m values, and that interdispersed between them are rather intricate dynamic behaviors, such as quasi-periodic oscillations (case V in Figure 11) at $\Theta_m = 0.03814$ and period 5 oscillations (case VI in Figure 11) for $\Theta_m = 0.03813$. The five loops form a rather thin band with a small but distinct bandwidth, suggesting that a second frequency (2-torus) contributes to the dynamic behavior. Following the period-5 solutions, a region with chaotic behavior occurs (not shown). Further decreasing of Θ_m leads to period-4 oscillations (case VII at $\Theta_m = 0.038$) followed by a third chaotic band (VIII). In a small band around $\Theta_m = 0.0376$, oscillations of period-3 (case IX in Figure 11) occur and lead to chaos followed by a shift to a steady-state region when the inlet temperature is further decreased. In contrast to the findings of Jorgensen and Aris (1983) for a CSTR with two consecutive reactions, we did not find period-doubling cascades from the period-5 and period-3 solutions for the CSDR model. Figure 11 shows that in cases VII to IX a large-amplitude oscillation (burst) is followed by several small-amplitude oscillations. The chaotic motion in case VIII consists of an aperiodic sequence of four small peaks followed by a large peak and three small peaks, suggesting a homoclinic chaos in this parameter region rather than a chaos occurring by period doubling.

It is known (Boe and Chang, 1989) that PI control can itself generate complex dynamics, especially when coupled to an open-loop unstable system. The control-gains P_3 and P_4 were selected such that the reactor dynamics were not affected by the impact of the controller.

Loci of singular points of codimension 1, plotted in the plane of an operating or design variable vs. a bifurcation parameter, enable rapid determination of all the qualitatively different bifurcation diagrams that can be attained for different values of the operating or design variables. Thus, we used the Δ vs. Θ_m map shown in Figure 5 to construct Figure 6, showing all the different Θ vs. Θ_m bifurcation diagrams that can be obtained for different cooling capacities. In applications, it is often necessary to predict the impact of changing two design or operating parameters on the qualitative features of the bifurcation diagram. This requires construction of loci of singular points of codimension 2. This procedure and its advantages are described in the next section.

Mapping Regions with Qualitatively Different Bifurcation Diagrams

We describe here the construction of maps in the plane of two design or operating variables, say p_1 and p_2, of regions in which the bifurcation diagrams of Θ vs. Θ_m have qualitatively different steady-state and/or dynamic features. The

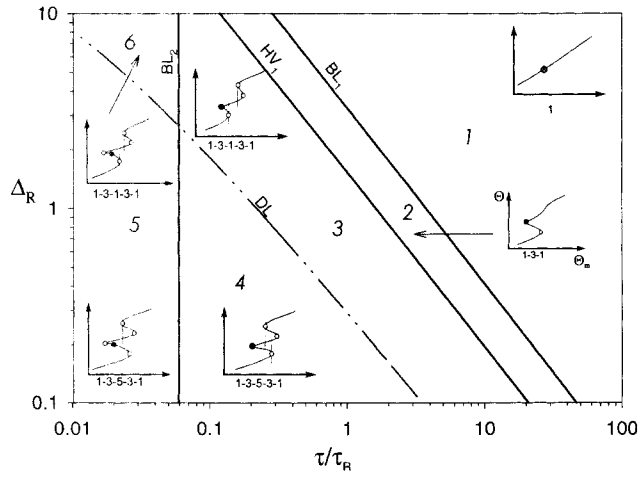

Figure 12. Division of the Δ_R vs. τ/τ_R plane into six regions with qualitatively different Θ vs. Θ_m steady-state bifurcation diagrams by codimension-2 singular points.

HV = hysteresis, DL = double limit, BL = boundary limit. The six corresponding bifurcation diagrams are shown as insets.

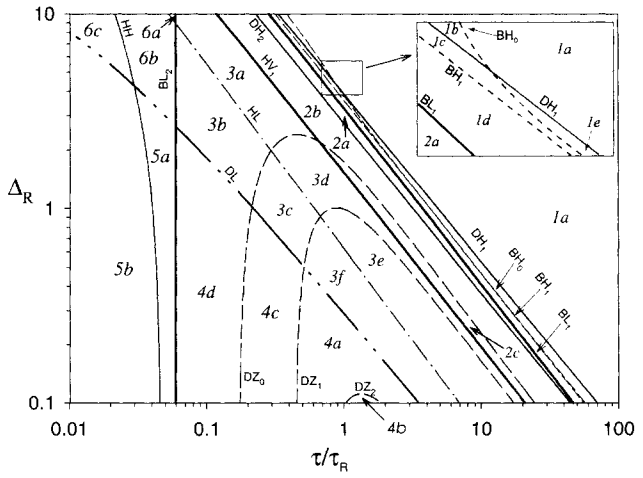

Figure 13. Division of the Δ_R vs. τ/τ_R plane into regions with qualitatively different Θ vs. Θ_m dynamic bifurcation diagrams by the loci of steady-state and dynamic singular points of codimension 2.

HV = hysteresis, DL = double limit, BL = boundary limit, DZ = double-zero, DH = degenerate Hopf, HH = Hopf–Hopf mode interaction, HL = Hopf-limit, BH = boundary Hopf. Numbers distinguish between regions with different steady-state features (same as Figure 12); letters distinguish among regions with different dynamic features.

boundaries of these regions are loci of codimension-2 singular points. The various codimension-2 singularities and their unfoldings are described in Figure 3. Their mathematical definitions and associated calculation are reviewed in the Appendix.

We first describe the construction of regions having different steady-state bifurcation diagrams. This requires construction of the hysteresis (HV), double limit (DL), isola (I), and boundary limit (BL) varieties. Figure 12 shows the loci of these varieties for a Δ_R range of [0.1–10] and a τ/τ_R range of [0.01–100]. Note that an I variety does not exist in this region. It does, however, exist for the unpractical range of $\tau/\tau_R < 0.01$ which is discussed later. The four varieties shown in Figure 12 generate six different regions, each with qualitatively different steady-state bifurcation diagrams of Θ vs. Θ_m. In region 1, which is to the right of BL_1, a unique steady state exists for all Θ_m values. A 1-3-1 multiplicity pattern exists for (Δ_R, τ/τ_R) values in region 2, bounded between the BL_1 and H_1 varieties. In regions 3 and 6, the bifurcation diagrams contain two separate regions with three solutions, while in regions 4 and 5 the multiplicity pattern is 1-3-5-3-1. In regions 2, 3, and 4, the breakthrough locus acts like a limit point, whereas in regions 5 and 6 a separate limit-point is formed. The different steady-state bifurcation diagrams are shown as insets in the figure.

We showed in the previous section that dynamic instabilities may preclude operation at a desirable steady-state solution. Thus, it is essential to differentiate among steady-state bifurcation diagrams having qualitatively different stability features. This is accomplished by constructing loci of codimension-2 singular points separating regions with different dynamic features. We illustrate this by Figure 13, which includes not only the four varieties shown in Figure 12, but also the loci of the double-zero (DZ), degenerate Hopf (DH), Hopf–Hopf mode-interaction (HH), and some of the Hopf-limit (HL) points. These loci divide the (Δ_R, τ/τ_R) plane into 23 subregions. The corresponding bifurcation diagrams are shown in Figure 14. The numbers distinguish between regions with different steady-state features (same as Figure 12), while letters characterize regions with different dynamic features. Region 1a is the only one for which a unique, stable state exists for all Θ_m. However, operation in this region may not be economical due to the need for either very high cooling capacity or high residence time. In regions 1b–1e, a unique steady state exists over the whole temperature range, but it is unstable over a bounded range of Θ_m. In regions 2a, 2b, and 2c, which show a 1-3-1 multiplicity, stable steady states with a high yield of the desired product may be obtained.

Inspection of the bifurcation diagrams points out the importance of determining the HL variety. At this global singularity, a Hopf and a limit point interchange their relative position (see Figure 3). Crossing such an HL variety leads, for example, to the transition between cases 3a and 3b, 3c and 3d, 3e and 3f, or 6a and 6b (Figure 14). While a *unique*, stable, high-yield steady state exists for some Θ_m in 3a, 3d, 3e, and 6a, these states do not exist after the crossing of the HL variety.

Maps of the type presented in Figure 13 provide a reactor designer with important insights into the dynamics of the CSDR. They help the designer select desirable regions of operation and design a robust control policy, which prevents a drift to an undesired state if this exists in addition to the desired one.

Simulations indicate that for very short and unrealistic residence times (e.g., $\tau/\tau_R < 10^{-2}$) new behavioral features are generated, which are mainly of academic interest. These include the existence of isolated solution branches, seven steady-state solutions, and infinite limit points at which a limit

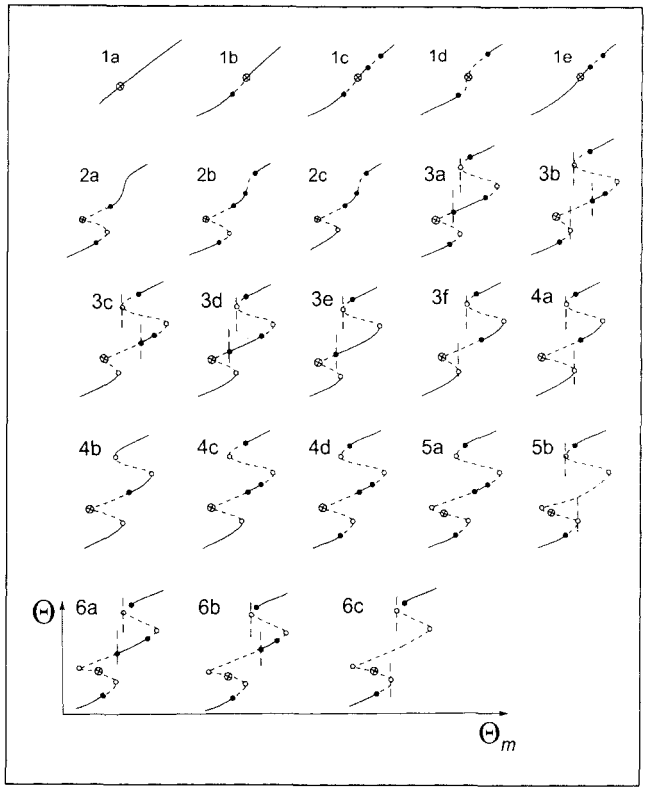

Figure 14. Dynamic bifurcation diagrams corresponding to the 23 regions in Figure 13.

● = Hopf point, ○ = limit point, ⊗ = breakthrough.

point appears (or disappears) as $\Theta_m \to \infty$. As the validity of the decanting model is questionable under these conditions, we avoid discussing these rather quaint curiosities.

Concluding Remarks

The CSDR has distinct advantages for conducting certain two-phase reactions. One important benefit of this operation is that one phase is completely consumed in the reactor, decreasing the effort involved in treating the effluent and undesired byproducts. Another important advantage is the removal of the desired product into another phase, in which the rate of the undesired consecutive reaction is much lower. Thus, this operation may enhance the yield of the desired product, increase the safety of the process, and minimize the need to treat the effluent and byproducts. Clearly, this operation is not suitable or advantageous for all two-phase reactions, but it merits evaluation and consideration for specific applications.

The analysis and numerical results illustrate that dynamic constraints may complicate the operation of a CSDR in which exothermic reactions occur. Clearly, the temperature dependence of the heat-removal from the reactor must exceed that of the heat-generation. Unfortunately, for stability, this simple and intuitive condition is merely necessary, not sufficient. The simulations indicate that in many situations, a state that satisfies the slope condition is unstable. The dynamic considerations may have a strong impact on the heat management and the control policy needed to prevent excursions to undesired or dangerous regions of operation.

The effluent composition of a CSDR operating at a specific Θ is independent of the cooling capacity and feed and coolant temperature. Thus, if a desired steady state is unstable, one may still get a stable steady state with the same effluent composition by increasing the heat-exchange area and/or increasing the coolant temperature to get the same reactor temperature. This may substantially increase the price of the reactor, especially when the reacting mixture is corrosive. It should be noted that both the numerical examples and pilot-plant data are for a highly exothermic reaction system. Many of the dynamic stability constraints found in the specific example we considered may not exist for reaction systems with milder heats of reaction.

Simulations of the proprietary reaction system underscored the importance of the reactor dynamics and operability issues. For example, steady-state calculations showed that feasible decanter operation could be achieved using a reactor-to-coolant driving force as large as 50°C. This large driving force enabled use of a relatively small heat exchanger, but it led to oscillations and extreme parametric sensitivity to perturbations. A temperature difference of less than 10°C is needed to guarantee stable operation. Further, to avoid sensitivity to perturbations, a heat-exchange area more than double that needed for stable operation is required. Reactor stability could be enhanced by feedback control of the reactor temperature, with the coolant temperature as the manipulated variable. Given the extreme energetics of the reaction system, however, an oversized heat-exchanger and small cooling driving force are recommended in the event of a failure of the cooling system.

Our model does not account for the dynamics and efficiency of the decanting operation or possible phase inversion. Including these will place another constraint on the minimal residence time in the CSDR. The examples and pilot-plant data indicate a sensitive dependence of the organic phase volume on the operating temperature of the CSDR. Thus, its efficient application may place strict constraints on the temperature range in which it can be operated.

The examples given earlier illustrate the useful insight about the design, operation, and control of a CSDR that one may gain by constructing maps of the loci of the various singular points, such as those presented in Figures 5 and 13. Using a numerical continuation technique, these loci can be computed efficiently and readily. The examples demonstrate that determination of global bifurcation, such as the HL point, provide important information that cannot be extracted from local analysis.

The model presented here includes some important simplifications, such as temperature-independent solubilities and transport coefficients and a highly simplified expression for the interfacial area. It ignores the dynamics and efficiency of the decanter. These simplifications, which may be removed, enabled an efficient determination and presentation of the main features of this novel reactor. Our analysis and pilot-plant data suggest that a CSDR may be a useful new tool in the arsenal of chemical reactor designers.

Acknowledgments

The financial support of the Austrian Science Foundation Grant No. J01173-TEC and ACS-PRF is gratefully acknowledged. We are very thankful to Prof. V. Balakotaiah for many helpful discussions.

Notation

a_0 = interphase area per total liquid volume when $V_I = V_{II}$, 1/m
A_h = heat-transfer area, m^2
$c_{i,j}$ = concentration of species i in phase j, kmol/m^3
$c_{i,j,f}$ = concentration of species i in feed of phase j, kmol/m^3
$c_{p,i}$ = heat capacity of species i, kJ/(kmol·K)
Da_i = Damköhler number of reaction i, Eq.
E_i = activation energy of reaction i, kJ/kmol
f = breakthrough factor, Eq. 17
$\boldsymbol{F} = \boldsymbol{C}^{-1} \cdot \boldsymbol{f}$
$\boldsymbol{g}$ = vector of model equations
h = overall heat transfer coefficient, kW/(m^2·K)
H_i = distribution coefficient of species i, $c^*_{i,I}/c^*_{i,II}$
$-\Delta H_i$ = heat of the reaction i, kJ/kmol
$\boldsymbol{J}^*$ = adjoint operator (conjugate transpose of $\boldsymbol{J}$)
k_i = rate constant of reaction i at T_r, m^3/(kmol·s)
k_{int} = integral control constant, $1/s^2$
k_m = overall mass-transfer coefficient, m/s
k_v = drainage valve constant, 1/s
$n_{i,j}$ = accumulation of component i in phase j, kmol
$\boldsymbol{p}$ = m-dimensional parameter vector
q_i = dimensionless effluent flow rate of phase i
r_i = reaction rate of reaction, i, kmol/(m^3·s)
$\hat{r}_i$ = dimensionless rate expression of reaction i, Eq. A1
R = universal gas constant, kJ/(kmol·K)
t = time, s
T_r = reference temperature (E/R), K
$\boldsymbol{u}$ = vector of variables
$v_{crit,i}$ = breakthrough constants
V_s = setpoint of the total volume, m^3
V_r = reactor volume, m^3
V_i = molar volume of component i, m^3/kmol
Y = yield of component D
β_i = adiabatic temperature rise of reaction I, Eq. 20
μ = eigenvalue
$\nu_{i,j}$ = stoichiometric coefficient of species i in reaction j
$\Phi_{1,2}$ = dimensionless groups, Eqs. A13–A14
σ = ratio of activation energies, E_2/E_1
τ = dimensionless residence time, Eq. 19
Θ = dimensionless temperature, RT/E
Ψ = dimensionless group, Eq. A15
Ω_i = dimensionless volume of phase I, Eq. 19
ω = dimensionless time, Eq. 19

Subscripts

c = coolant
f = feed
m = weighted average
I, R = imaginary, real part
R = reference value, corresponding to a typical operation situation

Literature Cited

Balakotaiah, V., and D. Luss, "Structure of the Steady-State Solutions of Lumped-Parameter Chemically Reacting Systems," *Chem. Eng. Sci.*, **37**, 1611 (1982).

Balakotaiah, V., and D. Luss, "Multiplicity Features of Reacting Systems: Dependence of the Steady States of a CSTR on the Residence Time," *Chem. Eng. Sci.*, **38**, 1709 (1983).

Balakotaiah, V., and D. Luss, "Global Analysis of the Multiplicity Features of Multi-Reaction Lumped-Parameter Models," *Chem. Eng. Sci.*, **39**, 865 (1984).

Balakotaiah, V., and D. Luss, "Global Mapping of Parameter Regions with a Specific Number of Solutions," *Chem. Eng. Sci.*, **43**, 957 (1988).

Boe, E., and H.-S. Chang, "Dynamics of Delayed Systems under Feedback Control," *Chem. Eng. Sci.*, **44**, 1281 (1989).

Chow, S. N., and J. Hale, "Methods of Bifurcation Theory," *Grundlehren*, Springer-Verlag, New York, p. 251 (1982).

Farr, W. W., and R. Aris, "'Yet Who Would Have Known the Old Man to Have Had So Much Blood in Him'—Reflections on the Multiplicity of Steady States of the Stirred-Tank Reactor," *Chem. Eng. Sci.*, **41**, 1385 (1986).

Feigenbaum, M. J., "Universal Behavior in Nonlinear Systems," *Physica*, **7D**, 16 (1983).

Golubitsky, M., and B. L. Keyfitz, "A Qualitative Study of the Steady-State Solutions for a Continuously-Stirred Tank Chemical Reactor," *SIAM J. Math. Anal.*, **11**, 316 (1980).

Golubitsky, M., and D. G. Schaeffer, *Singularities and Groups in Bifurcation Theory*, Vol. 1, Springer-Verlag, New York (1985).

Harold, M. P., J. J. Ostermaier, D. W. Drew, J. J. Lerou, and D. Luss, "The Continuously-Stirred Decanting Reactor: Steady State and Dynamic Features," *Chem. Eng. Sci.*, **51**, 1777 (1996).

Hassard, B., N. Kazarinoff, and Y. H. Wan, "Theory and Applications of Hopf Bifurcation," *London Mathematical Society Lecture Notes Series*, **41**, Cambridge Univ. Press, Cambridge (1981).

Hopf, E., "Abzweigung einer Periodischen Lösung von einer Stationären Lösung eines Differentialsystems," *Ber. Math Phys. Sächsische Akad. Wiss. Leipzig*, **94**, 1 (1942).

Iooss, G., and D. D. Joseph, *Elementary Stability and Bifurcation Theory*, Springer-Verlag, New York (1981).

Jorgensen, D. V., and R. Aris, "On the Dynamics of a Stirred Tank with Consecutive Reactions," *Chem. Eng. Sci.*, **38**(1), 45 (1983).

Keller, H. B., "Numerical Solutions of Bifurcation and Nonlinear Eigenvalue Problems," *Applications of Bifurcation Theory*, P. H. Rabinowitz, ed., Academic Press, New York, p. 159 (1977).

Kollar, J., U.S. Patent No. 5,321,157 (1994).

Kubicek, M., and M. Marek, *Computational Methods in Bifurcation Theory and Dissipative Structures*, Springer-Verlag, New York (1983).

Piret, E. L., W. H. Penney, and P. J. Trambouze, "Extractive Reaction: Batch and Continuous-Flow Chemical Reaction Systems, Dilute Case," *AIChE J.*, **6**, 394 (1960).

Subramanian, S., and V. Balakotaiah, "Classification of Steady-State and Dynamic Behavior of Distributed Reactor Models," *Chem. Eng. Sci.*, **51**, 401 (1996).

Subramanian, S., and V. Balakotaiah, "Classification of Steady-State and Dynamic Behavior of a Well-Mixed Heterogeneous Reactor Model," *Chem. Eng. Sci.*, **52**, 961 (1997).

Trambouze, P. J., and E. L. Piret, "Extractive Reaction: Batch- and Continuous-Flow Chemical Reaction Systems, Concentrated Case," *AIChE J.*, **6**, 574 (1960).

Trambouze, P. J., M. T. Trambouze, and E. L. Piret, "Chemical Reaction Processes in Two-Phase Systems: Theory and Experimental Results for Slow Chemical Reactions in Batch, Column, and Continuous Stirred Tank Reactor Operations," *AIChE J.*, **7**, 138 (1961).

Trambouze, P. J., "Calcul des reacteurs pour la mise en ouevre de reactions ou deux phases liquides interviennent," *Chem. Eng. Sci.*, **14**, 161 (1961).

Uppal, A., W. H. Ray, and A. B. Poore, "On the Dynamic Behavior of Continuous Stirred Tank Reactors," *Chem. Eng. Sci.*, **29**, 967 (1974).

Uppal, A., W. H. Ray, and A. B. Poore, "The Classification of the Dynamic Behavior of Continuous Stirred Tank Reactors—Influence of Reactor Residence Time," *Chem. Eng. Sci.*, **31**, 205 (1976).

Vaganov, D. A., N. G. Samoilenko, and V. G. Abramov, "Periodic Regime of Continuous Stirred Tank Reactors," *Chem. Eng. Sci.*, **33**, 1133 (1978).

Warwel, S., and M. R. G. Klass, U.S. Patent No. 5,321,158 (1994).

Westerterp, K. R., "Multifunctional Reactors," *Chem. Eng. Sci.*, **47**(9), 215 (1992).

Appendix

Dimensionless model equations

Introducing the variables defined by Eq. 19 into the dimensional model equations, Eqs. 2 and 4–18, the following dimensionless equations are obtained:

$$\hat{r}_1 = Da_1 \exp\left(1 - \frac{1}{\Theta}\right) \cdot u_{A,\mathrm{I}} \cdot u_{B,\mathrm{I}},$$

$$\hat{r}_2 = Da_2 \exp\left(\sigma - \frac{\sigma}{\Theta}\right) \cdot u_{B,\mathrm{II}} \cdot u_{D,\mathrm{II}}. \quad \text{(A1)}$$

Mass Balance: Phase I

$$\frac{d(u_{A,\mathrm{I}}\Omega_\mathrm{I})}{d\omega} = 1 - q_\mathrm{I} u_{A,\mathrm{I}} + \nu_{A,1} \cdot \hat{r}_1 \cdot \Omega_\mathrm{I} \quad \text{(A2)}$$

$$\frac{d(u_{B,\mathrm{I}}\Omega_\mathrm{I})}{d\omega} = \frac{c_{B,\mathrm{I},f}}{c_{B,\mathrm{II},f} H_B} - q_\mathrm{I} u_{B,\mathrm{I}} + \nu_{B,1} \hat{r}_1 \Omega_\mathrm{I} \cdot \frac{c_{A,\mathrm{I},f}}{c_{B,\mathrm{II},f} H_B} + (u_{B,\mathrm{II}} - u_{B,\mathrm{I}})(\Omega_\mathrm{I} + \Omega_\mathrm{II}) \frac{P_2}{H_B} \quad \text{(A3)}$$

$$\frac{d(u_{C,\mathrm{I}}\Omega_\mathrm{I})}{d\omega} = 1 - q_\mathrm{I} u_{C,\mathrm{I}} + (u_{C,\mathrm{II}} - u_{C,1})(\Omega_\mathrm{I} + \Omega_\mathrm{II}) \frac{P_2}{H_C} \quad \text{(A4)}$$

$$u_{A,\mathrm{I}} + u_{B,\mathrm{I}} \frac{c_{B,\mathrm{II},f} H_B}{c_{A,\mathrm{I},f}} \frac{\hat{V}_B}{\hat{V}_A} + u_{C,\mathrm{I}} \frac{c_{C,\mathrm{I},f}}{c_{A,\mathrm{I},f}} \frac{\hat{V}_C}{\hat{V}_A} = \frac{1}{\hat{V}_A c_{A,\mathrm{I},f}}. \quad \text{(A5)}$$

Mass Balance: Phase II

$$\frac{d(u_{B,\mathrm{II}}\Omega_\mathrm{II})}{d\omega} = P_1 - P_1 q_\mathrm{II} u_{B,\mathrm{II}} - P_2(u_{B,\mathrm{II}} - u_{B,\mathrm{I}})(\Omega_\mathrm{I} + \Omega_\mathrm{II}) + \nu_{B,2} \hat{r}_2 \Omega_\mathrm{II} \quad \text{(A6)}$$

$$\frac{d(u_{C,\mathrm{II}}\Omega_\mathrm{II})}{d\omega} = P_1 \frac{c_{C,\mathrm{II},f} H_C}{c_{C,\mathrm{I},f}} - P_1 q_\mathrm{II} u_{C,\mathrm{II}} - P_2(u_{C,\mathrm{II}} - u_{C,\mathrm{I}})(\Omega_\mathrm{I} + \Omega_\mathrm{II}) \quad \text{(A7)}$$

$$\frac{d(u_{D,\mathrm{II}}\Omega_\mathrm{II})}{d\omega} = P_1 \frac{c_{D,\mathrm{II},f}}{c_{B,\mathrm{II},f}} - P_1 q_\mathrm{II} u_{D,\mathrm{II}} + \nu_{D,1} \hat{r}_1 \Omega_\mathrm{I} \cdot \frac{c_{A,\mathrm{I},f}}{c_{B,\mathrm{II},f}} + \nu_{D,2} \hat{r}_2 \Omega_\mathrm{II} \quad \text{(A8)}$$

$$\frac{d(u_{E,\mathrm{II}}\Omega_\mathrm{II})}{d\omega} = P_1 - P_1 q_\mathrm{II} u_{E,\mathrm{II}} + \nu_{E,1} \hat{r}_1 \Omega_\mathrm{I} \cdot \frac{c_{A,\mathrm{I},f}}{c_{E,\mathrm{II},f}} + \nu_{E,2} \hat{r}_2 \Omega_\mathrm{II} \quad \text{(A9)}$$

$$\frac{d(u_{F,\mathrm{II}}\Omega_\mathrm{II})}{d\omega} = P_1 \frac{c_{F,\mathrm{II},f}}{c_{B,\mathrm{II},f}} - P_1 q_\mathrm{II} u_{F,\mathrm{II}} + \nu_{F,2} \hat{r}_2 \Omega_\mathrm{II} \quad \text{(A10)}$$

$$u_{B,\mathrm{II}} + u_{C,\mathrm{II}} \frac{c_{C,\mathrm{I},f}}{H_C c_{B,\mathrm{II},f}} \frac{\hat{V}_C}{\hat{V}_B} + u_{D,\mathrm{II}} \frac{\hat{V}_D}{\hat{V}_B} + u_{E,\mathrm{II}} \frac{c_{E,\mathrm{II},f} \hat{V}_E}{c_{B,\mathrm{II},f} \hat{V}_B} + u_{F,\mathrm{II}} \frac{\hat{V}_F}{\hat{V}_B} = \frac{1}{\hat{V}_B c_{B,\mathrm{II},f}}. \quad \text{(A11)}$$

Energy Balance

$$\frac{\Phi_1\Omega_1 + \Phi_2\Omega_2}{\Psi} \frac{\partial\Theta}{\partial\omega} = \Delta \cdot \frac{\tau}{\tau_R} \cdot (\Theta_c - \Theta) + (\Theta_f - \Theta) + \frac{1}{\Psi}\left(\frac{c_{A,\mathrm{I},f}}{c_{B,\mathrm{II},f}} \hat{r}_1 \cdot \Omega_\mathrm{I} + \hat{r}_2 \cdot \Omega_\mathrm{II}\right) \quad \text{(A12)}$$

$$\Phi_1 = \left(\frac{c_{A,\mathrm{I},f}}{c_{B,\mathrm{II},f}} u_{A,\mathrm{I}} + \frac{c_{pB}}{c_{pA}} H_B u_{B,\mathrm{I}} + \frac{c_{pC}}{c_{pA}} \frac{c_{C,\mathrm{I},f}}{c_{B,\mathrm{II},f}} u_{C,\mathrm{I}}\right) \quad \text{(A13)}$$

$$\Phi_2 = \left(\frac{c_{pB}}{c_{pA}} u_{B,\mathrm{II}} + \frac{c_{pC}}{c_{pA}} \frac{c_{C,\mathrm{II},f}}{c_{B,\mathrm{II},f} H_C} u_{C,\mathrm{II}} + \frac{c_{pD}}{c_{pA}} u_{D,\mathrm{II}} + \frac{c_{pE}}{c_{pA}} \frac{c_{E,\mathrm{II},f}}{c_{B,\mathrm{II},f}} u_{E,\mathrm{II}} + \frac{c_{pF}}{c_{pA}} u_{F,\mathrm{II}}\right) \quad \text{(A14)}$$

$$\Psi = \frac{c_{A,\mathrm{I},f}}{c_{B,\mathrm{II},f}} + \frac{c_{pB}}{c_{pA}} \frac{c_{B,\mathrm{I},f}}{c_{B,\mathrm{II},f}} + \frac{c_{pC}}{c_{pA}} \frac{c_{C,\mathrm{I},f}}{c_{B,\mathrm{II},f}} + P_1\left(\frac{c_{pB}}{c_{pA}} + \frac{c_{pC}}{c_{pA}} \frac{c_{C,\mathrm{II},f}}{c_{B,\mathrm{II},f}} + \frac{c_{pD}}{c_{pA}} \frac{c_{D,\mathrm{II},f}}{c_{B,\mathrm{II},f}} + \frac{c_{pE}}{c_{pA}} \frac{c_{E,\mathrm{II},f}}{c_{B,\mathrm{II},f}}\right). \quad \text{(A15)}$$

Breakthrough

$$\frac{q_\mathrm{I}}{q_\mathrm{II}} = \begin{cases} 0 & \text{for} \quad \Omega_\mathrm{II}/(\Omega_\mathrm{I} + \Omega_\mathrm{II}) > \upsilon_{\mathrm{crit},1} \\ f \cdot P_1 \cdot \Omega_\mathrm{I}/\Omega_\mathrm{II} & \text{for} \quad \upsilon_{\mathrm{crit},2} < \Omega_\mathrm{II}/(\Omega_\mathrm{I} + \Omega_\mathrm{II}) < \upsilon_{\mathrm{crit},1} \\ P_1 \cdot \Omega_\mathrm{I}/\Omega_\mathrm{II} & \text{for} \quad \upsilon_{\mathrm{crit},2} > \Omega_\mathrm{II}/(\Omega_\mathrm{I} + \Omega_\mathrm{II}) \end{cases} \quad \text{(A16)}$$

$$f = 2x^3 - 3x^2 + 1 \quad \text{with} \quad x = \frac{\Omega_\mathrm{II}/(\Omega_\mathrm{I} + \Omega_\mathrm{II}) - \upsilon_{\mathrm{crit},2}}{\upsilon_{\mathrm{crit},1} - \upsilon_{\mathrm{crit},2}}. \quad \text{(A17)}$$

Level Control

$$\frac{1}{P_1} q_\mathrm{I} + q_\mathrm{II} = P_3(\Omega_1 + \Omega_2) + P_4 \int_0^\omega [(\Omega_1(\omega') + \Omega_2(\omega') - \Omega_s]\, d\omega' \quad \text{(A18)}$$

Interphase Area

$$P_2(\tau) = 4P_{2,R} \cdot \frac{\tau}{\tau_R} \cdot \frac{\Omega_\mathrm{I}\Omega_\mathrm{II}}{(\Omega_\mathrm{I} + \Omega_\mathrm{II})^2} \quad \text{(A19)}$$

Singular points definition and computation

We consider only cases in which (1) the nonlinear function f is a single-valued vector function of u and is smooth (differentiable to all orders) with respect to u and λ within the feasible region, and (2) the branches of solutions do not intersect. All these conditions are satisfied by the CSDR model.

The boundaries of parameter regions with qualitatively similar bifurcation diagrams may be determined by application of the *singularity theory with a distinguished parameter*, developed by Golubitsky and Schaeffer (1985). They proved that the qualitative steady-state features of the local bifurcation diagrams of $f(u, p, \lambda) = 0$, which satisfy the conditions just given, may change only if the parameter set crosses one of three hypersurfaces in the parameter space of the unfolding parameters: *hysteresis*, *double limit*, and *isola* variety. The bifurcation diagrams obtained by the unfolding of these three steady-state codimension-2 varieties are shown in Figure 3.

Golubitsky and Keyfitz (1980) used this method to predict all the qualitatively different bifurcation diagrams of a cooled CSTR. Balakotaiah and Luss (1982, 1983, 1984, 1988) used the three varieties to divide the global parameter space of lumped reactor models into regions with qualitatively different steady-state bifurcation diagrams. Farr and Aris (1986) used it to classify the bifurcation diagrams of a CSTR in which two reactions occur. Subramanian and Balakotaiah (1996, 1997) applied these methods to classify the steady-state and dynamic features of various reactor models.

The *hysteresis variety* (HV) is defined by the set of conditions:

$$f(u, p, \lambda) = 0 \tag{A20}$$

$$J(u, p, \lambda) \cdot y = 0 \tag{A21}$$

$$J^*(u, p, \lambda) \cdot v = 0 \tag{A22}$$

$$\langle v, D^2_{uu} f(u, p, \lambda) \cdot (y, y) \rangle = 0 \tag{A23}$$

$$\langle y, v \rangle = 1, \tag{A24}$$

where $\langle \cdot, \cdot \rangle$ denotes the standard inner product, J is the Jacobian matrix of f, the superscript $*$ denotes the conjugate transpose, y and v are the eigenvector and adjoint eigenvector of J, and

$$D^2_{uu} f(u, p, \lambda) \cdot (y, y) = \sum_{i=1}^{n} \sum_{j=1}^{n} \frac{\partial^2 f}{\partial u_i \partial u_j} y_i y_j. \tag{A25}$$

The preceding set of $3n+2$ equations determines the $3n$ variables (u, y, v), λ, and an additional parameter p_1 in p.

An *isola variety* (I) satisfies the conditions:

$$f(u, p, \lambda) = 0 \tag{A26}$$

$$J^*(u, p, \lambda) \cdot v = 0 \tag{A27}$$

$$\langle v, D_\lambda f(u, p, \lambda) \rangle = 0 \tag{A28}$$

$$\langle v, v \rangle = 1. \tag{A29}$$

These $2n+2$ equations determine $2n$ variables (u, v), λ, and an additional parameter in p at an elliptic or hyperbolic isola variety (Figure 3). The existence of an isola variety depends on the choice of the bifurcation variable.

A *double limit variety* (DL) is defined as the set of parameters at which two distinct limit points exist for the same value of λ (Figure 3). A limit point satisfies Eqs. A20, A21, and $\langle y, y \rangle = 1$. A double limit point satisfies the conditions:

$$f(u^{(i)}, p, \lambda) = 0 \quad i = 1, 2 \tag{A30}$$

$$J(u^{(i)}, p, \lambda) \cdot y^{(i)} = 0 \quad i = 1, 2 \tag{A31}$$

$$\langle y^{(i)}, y^{(i)} \rangle = 1 \quad i = 1, 2. \tag{A32}$$

The superscript $i = 1, 2$ denote the two distinct limit points. These $4n+2$ equations determine $4n$ variables ($u^{(1)}$, $u^{(2)}$, $y^{(1)}$, $y^{(2)}$), λ, and an additional parameter in p.

The *boundary limit* variety (BL) is the locus at which both a limit point and a breakthrough point exist. An *infinite limit* point (IL) is the set of parameters at which a limit point exists as $\lambda \to \infty$.

A dynamic bifurcation analysis determines the parameters at which the dynamic features of the system change. Uppal et al. (1974, 1976) and Vaganov et al. (1978) were the first to apply this technique to map the dynamic features of a CSTR. A steady state becomes unstable and periodic solutions appear at a *Hopf bifurcation* (Hopf, 1942; Hassard et al., 1981; Iooss and Joseph, 1981; Chow and Hale, 1982; Golubitsky and Schaeffer, 1985), which is of codimension 1, since only the bifurcation parameter is fixed. At that point a conjugate pair of eigenvalues μ of the linearization of Eq. 23, that is,

$$J(u, p, \lambda) y = \mu C y \tag{A33}$$

crosses the imaginary axis, while the real parts of the other eigenvalues are negative and

$$\frac{d\,\mathrm{Re}(\mu)}{d\lambda} \neq 0, \qquad \mathrm{Im}(\mu) \leq 0. \tag{A34}$$

The conditions for a Hopf point are Eq. A33, the steady-state condition (Eq. A20), and

$$\mathrm{Re}(\mu) = 0. \tag{A35}$$

Again, the norm of y may be chosen arbitrarily, say

$$\langle y, y \rangle = 1 + i. \tag{A36}$$

The preceding $2n+2$ (complex) conditions determine $2n$ variables (u, y) as well as μ and λ.

Two Hopf points coalesce at a *degenerate Hopf* point (DH) by violating the first condition in Eq. A34 (Golubitsky and Schaeffer, 1985). By perturbing one parameter of a degenerate Hopf point, we find either two Hopf points or none in the corresponding bifurcation diagram (Figure 3). The degenerate Hopf locus is located at a tangential intersection of the complex pair of eigenvalues with the imaginary axis [$\mathrm{Re}(\mu) = 0$], as shown in Figures A1a and A1b. At this point

$$f(u, p, \lambda) = 0 \tag{A37}$$

$$A(u, p, \lambda) \cdot y = -\mathrm{Im}(\mu) y \tag{A38}$$

$$A^T v = \mathrm{Im}(\mu) v \tag{A39}$$

$$\mathrm{Re}\left(\frac{v^* A_\lambda y}{v^* y} \right) = 0 \tag{A40}$$

$$\langle y, v \rangle = 1 + i, \tag{A41}$$

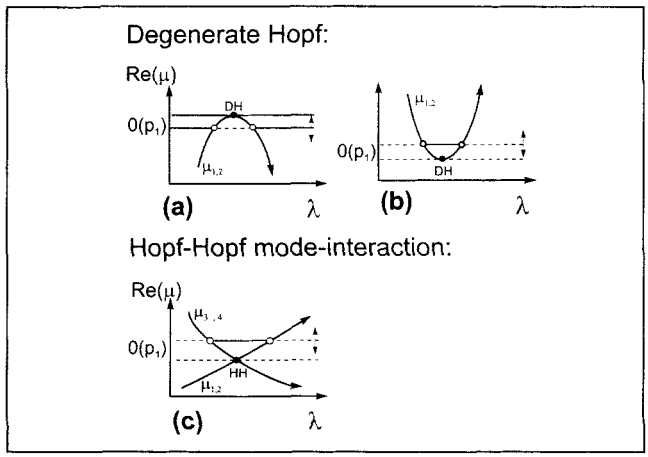

Figure A1. Dependence of the dominant eigenvalues on λ next to a degenerate Hopf and Hopf-Hopf mode-interaction.

where Eq. A40 implies violation of condition A34. The superscript $*$ denotes a conjugate transpose of the adjoint eigenvector. It is implicitly assumed that at the degenerate Hopf point condition Eq. A35 is satisfied. A_λ is the total derivative of the Jacobian matrix A. Note that since the capacitance matrix C in the CSDR model also depends on the state variables, the Jacobian matrix A has to be used, where

$$A = \frac{\partial(C^{-1}f)}{\partial u}\bigg|_{u,\lambda} = \left[\frac{\partial F}{\partial u_1} \cdots \frac{\partial F}{\partial u_n}\right]. \tag{A42}$$

The set of $3n+3$ (complex) equations, A35, A37–A41, is used to determine the $3n$ variables (u, y, v), the eigenvalue μ, the bifurcation parameter λ, and an additional parameter p_1.

At a *Hopf–Hopf mode-interaction* point (HH) two distinct conjugate pairs of eigenvalues intersect transversally the imaginary axis (see Figure A1c). At this point

$$f(u, p, \lambda) = 0 \tag{A43}$$

$$A(u, p, \lambda)\cdot y^{(1)} = \mu_1 y^{(1)} \tag{A44}$$

$$A(u, p, \lambda)\cdot y^{(2)} = \mu_2 y^{(2)} \tag{A45}$$

$$\mathrm{Re}(\mu_1) = \mathrm{Re}(\mu_2) = 0 \tag{A46}$$

$$\langle y^{(1)}, y^{(1)}\rangle = 1 + i \tag{A47}$$

$$\langle y^{(2)}, y^{(2)}\rangle = -1 + i \tag{A48}$$

where

$$\mathrm{Im}(\mu_1) \neq \mathrm{Im}(\mu_2) \neq 0. \tag{A49}$$

The set of $3n+4$ complex equations, Eqs. A43–A48, defines the $3n$ variables (u, $y^{(1)}$, $y^{(2)}$), μ_1, μ_2, λ, and one additional parameter in p (codimension 2). It is worth noting that in the unfoldings of a degenerate Hopf locus, the states bounded between the two Hopf points may be either stable or unstable, as shown in Figure A1, since the conjugate complex pair of eigenvalues $\mu_{1,2}$ approaches the imaginary axis either from the stable part of the plane ($\mathrm{Re}(\mu_{1,2}) < 0$, Figure A1a) or from the unstable part [$\mathrm{Re}(\mu_{1,2}) > 0$, Figure A1b]. In contrast, the transversal intersection at the Hopf–Hopf mode-interaction locus is such that, upon unfolding, the steady states bounded between the two Hopf points are either stable or no pair of Hopf points is created (Figure A1c). In addition, the Hopf–Hopf mode-interaction locus does not depend on the choice of the bifurcation parameter, while the degenerate Hopf locus does.

A Hopf and a limit point coalesce at a *double-zero* point (DZ) (Figure 3), that is, a pair of purely complex conjugate eigenvalues vanishes as it coalesces with the zero eigenvalue of a limit point. Using the concept of generalized eigenvectors, the following conditions are satisfied at a double-zero point:

$$A(u, p, \lambda)\cdot y^{(1)} = 0 \tag{A50}$$

$$A(u, p, \lambda)\cdot y^{(2)} = y^{(1)} \tag{A51}$$

$$\langle y^{(1)}, y^{(1)}\rangle = 1 \tag{A52}$$

$$\langle y^{(2)}, y^{(2)}\rangle = -1. \tag{A53}$$

The steady-state equation (Eq. A20) and Eqs. A50–A53 form $3n+2$ conditions that determine the $3n$ variables (u, $y^{(1)}$, $y^{(2)}$), λ, and an additional parameter p_1 in p.

At a *boundary-Hopf* locus (BH) a Hopf locus coalesces with the feasible operation boundary (breakthrough).

The qualitative steady-state and dynamic features of a bifurcation diagram may change by crossing either a local or a global bifurcation point. These global bifurcations lead to qualitative changes in the global dynamic features of the CSDR. For example, a global bifurcation occurs at a *Hopf-limit* point (HL), where a limit point and a Hopf point exist on different solution branches for the same set of parameters. A typical situation is depicted in Figure 3.

The total derivative of A with respect to the distinguished parameter required in Eq. A40 is

$$A_\lambda = \frac{\partial A}{\partial \lambda} + \sum_{i=1}^{n} \frac{\partial A}{\partial u_i}\frac{\partial u_i}{\partial \lambda}. \tag{A54}$$

From $dF(u, \lambda)/d\lambda = 0$ we conclude that

$$\frac{\partial u}{\partial \lambda} = -A^{-1}\frac{\partial F}{\partial \lambda}. \tag{A55}$$

While it is relatively easy to numerically compute the Jacobian matrix of F, it is rather difficult to compute its second- or higher-order derivatives at sufficient accuracy as round-off

errors become significant. Thus, we determine these derivatives using the relations

$$\frac{\partial \boldsymbol{F}}{du_i} = \frac{\partial (\boldsymbol{C}^{-1}\boldsymbol{f})}{du_i} = \frac{\partial \boldsymbol{C}^{-1}}{du_i}\boldsymbol{f} + \boldsymbol{C}^{-1}\frac{\partial \boldsymbol{f}}{du_i} \tag{A56}$$

$$\frac{\partial \boldsymbol{A}}{\partial \lambda} = \left[\frac{\partial^2 \boldsymbol{F}}{\partial \lambda \partial u_1} \cdots \frac{\partial^2 \boldsymbol{F}}{\partial \lambda \partial u_n}\right] \tag{A57}$$

$$\frac{\partial^2 \boldsymbol{F}}{\partial \lambda \partial u_j} = \frac{\partial^2 \boldsymbol{C}^{-1}}{\partial \lambda \partial u_j}\boldsymbol{f} + \frac{\partial \boldsymbol{C}^{-1}}{\partial u_j}\frac{\partial \boldsymbol{f}}{\partial \lambda} + \frac{\partial \boldsymbol{C}^{-1}}{\partial \lambda}\frac{\partial \boldsymbol{f}}{\partial u_j} + \boldsymbol{C}^{-1}\frac{\partial^2 \boldsymbol{f}}{\partial \lambda \partial u_j} \tag{A58}$$

$$\frac{\partial \boldsymbol{C}^{-1}}{d\lambda} = -\boldsymbol{C}^{-1}\frac{\partial \boldsymbol{C}}{d\lambda}\boldsymbol{C}^{-1} \tag{A59}$$

$$\frac{\partial \boldsymbol{C}^{-1}}{du_j} = -\boldsymbol{C}^{-1}\frac{\partial \boldsymbol{C}}{du_j}\boldsymbol{C}^{-1} \tag{A60}$$

$$\frac{\partial^2 \boldsymbol{C}^{-1}}{\partial \lambda \partial u_j} = -\left\{\frac{\partial \boldsymbol{C}^{-1}}{\partial \lambda}\frac{\partial \boldsymbol{C}}{\partial u_j}\boldsymbol{C}^{-1} + \boldsymbol{C}^{-1}\frac{\partial^2 \boldsymbol{C}}{\partial \lambda \partial u_j}\boldsymbol{C}^{-1} + \boldsymbol{C}^{-1}\frac{\partial \boldsymbol{C}}{\partial u_j}\frac{\partial \boldsymbol{C}^{-1}}{\partial \lambda}\right\}. \tag{A61}$$

This scheme avoids the need to compute numerically second-order derivatives as analytical expressions for the derivatives of $\boldsymbol{C}$ and $\boldsymbol{f}$ with respect to the state variables, and the distinguished parameter can be readily determined. This procedure significantly improves the convergence of the solver.

Manuscript received June 11, 1997, and revision received Nov. 19, 1997.